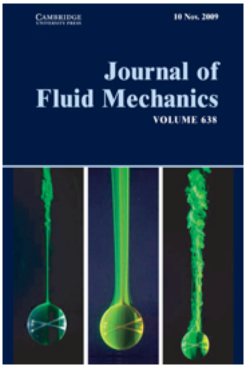

A higher-order Hele-Shaw approximation with application to gas flows through shallow micro-channels

A. D. GAT, I. FRANKEL and D. WEIHS

Journal of Fluid Mechanics / Volume 638 / November 2009, pp 141 - 160
DOI: 10.1017/S002211200999125X, Published online: 14 October 2009

Link to this article: http://journals.cambridge.org/abstract_S002211200999125X

How to cite this article:
A. D. GAT, I. FRANKEL and D. WEIHS (2009). A higher-order Hele-Shaw approximation with application to gas flows through shallow micro-channels. Journal of Fluid Mechanics, 638, pp 141-160 doi:10.1017/S002211200999125X

J. Fluid Mech. (2009), *vol.* 638, *pp.* 141–160. © Cambridge University Press 2009
doi:10.1017/S002211200999125X

A higher-order Hele-Shaw approximation with application to gas flows through shallow micro-channels

A. D. GAT†, I. FRANKEL AND D. WEIHS

Faculty of Aerospace Engineering, Technion – Israel Institute of Technology, Haifa 32000, Israel

(Received 28 April 2009; revised 16 July 2009; accepted 16 July 2009)

The classic hydrodynamic Hele-Shaw problem is revisited in the context of evaluating the viscous resistance to low-Mach compressible viscous gas flows through shallow non-uniform micro-fluidic configurations. Our recent study of gas flows through constricted shallow micro-channels indicates that the failure of the standard Hele-Shaw approximation to satisfy the no-slip boundary condition at the sidewalls severely restricts its applicability. To overcome this we have extended the asymptotic scheme to incorporate an inner solution in the vicinity of the sidewalls (which, in turn, allows for the characterization of the effects of channel cross-section geometry) and its matching to an outer correction. We have compared the results of the present asymptotic analysis to existing exact analytic and numerical results for straight and uniform channels and to finite-element simulations for a 90° turn and a symmetric T-junction, which demonstrate a remarkably improved accuracy relative to the standard Hele-Shaw approximation. This suggests the present scheme as a viable alternative for the rapid performance estimate of micro-fluidic devices.

1. Introduction

Gas flows through micro-channels appear in a variety of micro-fluidic applications (e.g. cooling in micro-electronic devices and flow control; see Ho & Tai 1998; Gad-El-Hak 1999). Typical of many of these micro-fluidic devices is that fluid motion takes place within the narrow gap between parallel solid walls (Lee, Wong & Zohar 2001; Yu *et al.* 2005). Furthermore, these configurations are often shallow in the sense that the gap width is much smaller than all other dimensions (Arkilic, Breuer & Schmidt 2001; Zohar *et al.* 2002). The small-Reynolds-number pressure-driven flows through these micro-configurations encounter a large viscous resistance giving rise to ‘low Mach compressibility’, i.e. substantial density variations accompanied by relatively minor gas accelerations (Taylor & Saffman 1957; Cole, Keller & Saffman 1967). Furthermore, under standard atmospheric conditions, gas flows through these micro-channels are characterized by Knudsen numbers $Kn \approx 10^{-2}$–10^{-1} and are thus subject to weak rarefaction effects (Cercignani 2000; Sone 2002).

The flow through long straight channels with a uniform cross-section has been studied extensively. An exact (series-form) analytic solution exists for the fully developed incompressible flow through such rectangular channels (cf. White 1986). Arkilic, Schmidt & Breuer (1997) have studied the lubrication approximation for

---

† Email address for correspondence: gat@tx.technion.ac.il

the compressible slip flow through a long two-dimensional micro-channel. Sharipov (1999) has studied gas flows through rectangular channels over the entire spectrum of the Knudsen numbers. Analytic solutions have been presented by Aubert & Colin (2001) and Jang & Wereley (2004) for slip flows (at small Kn) through the same configuration. However, many applications (e.g. channel networks and fuel-cell devices; Gad-El-Hak 2002; Lee, Wong & Zohar 2002*a*,*b*) involve more complex geometries including such elements as channel junctions and bifurcations and sudden expansions and contractions, among others. The study of non-uniform micro-channels is therefore of considerable interest.

Lauga, Stroock & Stone (2004) have analysed the small-Reynolds-number incompressible flow through slowly varying (quasi-uniform) planar channels. For shallow configuration progress may be made by considering Hele-Shaw flows within the narrow gap between parallel walls. These constitute a classic problem in fluid mechanics of considerable fundamental interest (transcending the immediate application to micro-channels). The basic problem formulation (cf. Batchelor 1967) is concerned with incompressible flows and is incapable of satisfying the no-slip boundary condition at the sidewalls. In our recent contribution (Gat, Frankel & Weihs 2008) we have extended the theory to viscous gas flows, still without accounting for the no-slip condition at the sidewalls. Comparison of our approximate analytic results and exact finite-element simulations has demonstrated that failure to satisfy this condition is the main source of error, effectively increasing it from the presumed quadratic to linear in the small shallowness parameter ε (defined in (2.4)). This, in turn, severely restricts the practical value of the resulting approximation to very small values of ε. It is thus expected that the extension of the classic Hele-Shaw approximation to incorporate the no-slip condition at the sidewalls can significantly enhance its usefulness. This constitutes the main thrust of the present contribution.

In the next section we formulate the problem and present the asymptotic scheme providing leading-order outer and inner approximations and a correction term to the former. Analytic closed-form solutions are obtained by use of conformal mapping. Also discussed in this section are the effects of weak rarefaction and non-rectangular cross-sections. In § 3 we digress from the non-uniform planform configurations at the focus of the present contribution to consider the flow through uniform micro-channels, which, in turn, provides an opportunity for comparison of our results with existing exact solutions. Subsequently, in § 4 we illustrate the scheme in the context of the flow through a 90° turn and a symmetric T-junction. In § 5 we recapitulate the main results. The effects of some specific cross-section geometries are explicitly presented in the Appendix.

2. Analysis

The steady motion of a perfect viscous gas is governed by the equation of continuity

$$\tilde{\nabla}\cdot(\tilde{\rho}\tilde{\boldsymbol{u}}) = 0, \tag{2.1}$$

the equation of motion (neglecting the effects of body forces)

$$\tilde{\rho}\tilde{\boldsymbol{u}}\cdot\tilde{\nabla}\tilde{\boldsymbol{u}} = -\tilde{\nabla}\tilde{p} + \tilde{\nabla}\cdot\tilde{\boldsymbol{\tau}}, \tag{2.2}$$

the equation of state

$$\tilde{p} = \tilde{\rho}R\tilde{T} \tag{2.3}$$

and the equation of energy (which, in anticipation of the subsequent isothermal-flow assumption, is not explicitly presented here). These equations are supplemented

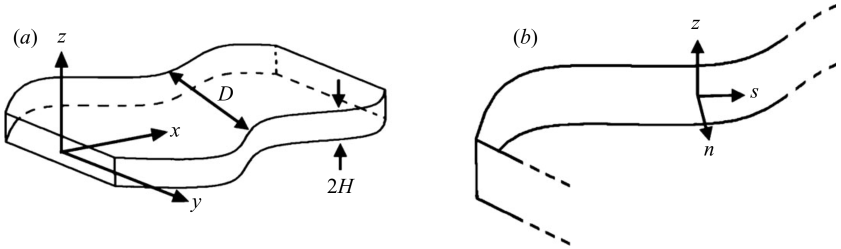

FIGURE 1. (*a*) Definition of coordinate system and geometrical parameters for shallow channels and (*b*) the local coordinates for the inner domain.

by appropriate boundary conditions. In (2.1)–(2.3), $\tilde{\rho}, \tilde{p}$ and $\tilde{T}$ denote the gas density, pressure and temperature, respectively; $\tilde{\boldsymbol{u}}$ is the fluid-velocity vector; $\tilde{\boldsymbol{\tau}}$ is the Newtonian stress tensor; and R is the gas constant.

To describe the flow through the narrow gap between parallel planes we employ a Cartesian coordinate system $(\tilde{x}, \tilde{y}, \tilde{z})$ whose $\tilde{x}$ and $\tilde{y}$ axes lie at the channel midplane and $\tilde{z}$ is perpendicular thereto (see figure 1). The $\tilde{x}$ and $\tilde{y}$ coordinates are normalized by D, a characteristic lateral dimension of the channel planform, whereas $\tilde{z}$ is normalized by H, half the gap width, to obtain the dimensionless coordinates x, y, z (tildes are omitted when denoting dimensionless quantities). Subsequent analysis focuses on shallow micro-channels, i.e. on the limit when

$$\varepsilon = \frac{H}{D} \ll 1. \tag{2.4}$$

For long shallow micro-channels whose uninsulated walls are maintained at uniform temperatures we follow the common practice in assuming an isothermal flow (see Arkilic *et al.* 1997; Qin, Sun & Yin 2007; see also the discussion in Gat *et al.* 2008) and that fluid-inertial effects are negligible (cf. Zohar *et al.* 2002; Graur, Meolans & Zeitoun 2005). We normalize the pressure by p_0, a characteristic pressure drop over a characteristic distance D in the streamwise direction. The corresponding reference density ρ_0 is selected by use of (2.3). The velocity scale reflecting the dominant balance between the pressure gradient and the viscous resistance is accordingly $U = p_0 H^2/\mu D$ (where μ denotes the shear viscosity of the fluid at the reference conditions). The x and y components of $\boldsymbol{u}$, u and v, respectively, are normalized by U; w, the corresponding z component, is scaled by εU.

2.1. *An outer expansion*

For the above scaling and asymptotically small ε we obtain from (2.1)–(2.3)

$$\frac{\partial}{\partial x}(\rho u) + \frac{\partial}{\partial y}(\rho v) + \frac{\partial}{\partial z}(\rho w) = 0, \tag{2.5}$$

$$\frac{\partial p}{\partial x} = \frac{\partial^2 u}{\partial z^2} + O(\varepsilon^2, \varepsilon Re), \tag{2.6}$$

$$\frac{\partial p}{\partial y} = \frac{\partial^2 v}{\partial z^2} + O(\varepsilon^2, \varepsilon Re), \tag{2.7}$$

$$\frac{\partial p}{\partial z} = O(\varepsilon^2, \varepsilon^3 Re) \tag{2.8}$$

and

$$p = \rho. \tag{2.9}$$

These are supplemented by the no-slip condition $\boldsymbol{u} = 0$ on the channel walls together with appropriate conditions at the channel entrance and exit sections. In (2.6)–(2.8) $Re = \rho_0 U H/\mu$ is the Reynolds number. Typical of the Hele-Shaw approximation is the appearance in the above equations of the reduced Reynolds number εRe rather than Re itself (cf. Batchelor 1967). Integrating (2.6) and (2.7) twice over z while making use of (2.8) and the no-slip conditions at $z = \pm 1$ we obtain the following for $\boldsymbol{u}_\parallel = (u, v)$:

$$\boldsymbol{u}_\parallel = -\frac{1}{2}\left(1 - z^2\right)\nabla_\parallel p, \tag{2.10}$$

where $\nabla_\parallel = \hat{\boldsymbol{\imath}}\partial/\partial x + \hat{\boldsymbol{\jmath}}\partial/\partial y$ is the planar portion of ∇. When defining

$$G = \frac{1}{6}p^2 \tag{2.11}$$

and making use of (2.9) and (2.10), integration yields

$$\int_0^1 \rho \boldsymbol{u}_\parallel \mathrm{d}z = -\nabla_\parallel G. \tag{2.12}$$

As such, G may represent the scalar potential of the mass-flux-density vector (per unit length) in the two-dimensional planform domain. Furthermore, substituting (2.9) and (2.10) in (2.5) we obtain

$$-\frac{3}{2}\left(1 - z^2\right)\nabla_\parallel^2 G + \frac{\partial}{\partial z}(pw) = 0. \tag{2.13}$$

When this relation is integrated across the channel and vanishing of w at $z = \pm 1$ is used, we find that $G(x, y)$ is harmonic, i.e.

$$\nabla_\parallel^2 G = 0 \tag{2.14}$$

within the planform domain formed by the intersection of the channel midplane and its sidewalls. We further conclude that in the absence of velocity slip at the walls, $w \equiv 0$ (see, however, § 2.4.1).

In subsequent analysis we focus on small Reynolds numbers and accordingly put forward the expansion

$$G \sim G_0 + \varepsilon \bar{c} G_1 + O\left(\varepsilon^2, \varepsilon Re\right), \tag{2.15}$$

where both G_0 and G_1 satisfy (2.14) and $\bar{c}$ is an $O(1)$ numerical coefficient to be defined later on (see (2.33) and (2.48)). By (2.10) in conjunction with the definition of G and its harmonic nature we cannot in general impose on the resulting solution the no-slip condition $\boldsymbol{u}_\parallel = 0$ at the channel sidewalls. Expansion (2.15) is thus expected to provide only an 'outer' solution becoming non-uniform in the vicinity of the sidewalls.

2.1.1. *Leading-order outer solution*

Following the above, we can only impose the vanishing at the channel sidewalls of the velocity components perpendicular thereto. By use of (2.10) and the definition of G, this is expressed by the condition

$$\frac{\partial G_0}{\partial n} = \hat{\boldsymbol{n}} \cdot \nabla_\parallel G_0 = 0 \tag{2.16}$$

(where $\hat{\boldsymbol{n}}$ is the unit vector lying in the midplane perpendicularly to the planform boundary and directed into the channel). To complete the formulation of the problem governing G_0 we need to specify the distribution of G_0 or $\partial G_0/\partial n$ across the entrance and exit sections of the channel. Subsequent calculation is facilitated via replacing these sections of the actual configuration by straight and uniform semi-infinite channels. In these we impose the far-field conditions

$$\frac{\partial G_0}{\partial n} = -\frac{C_j}{W_j}, \quad (j = 1, 2, \ldots). \tag{2.17}$$

Here $\partial/\partial n$ denotes differentiation along the cross-sectional normal directed into the channel and C_j and W_j are the dimensionless mass influx and channel width, respectively. (Evidently, by mass conservation $\sum_j C_j = 0$.) Condition (2.17) thus represents the far-field uniformity of the mass-flux density in these semi-infinite channels. The above well-posed Neumann problem uniquely determines $G_0(x, y)$ which is therefore considered a known function in subsequent derivation.

The actual calculation of G_0 may be facilitated by regarding it as the real part of an analytic function $F_0(t) = G_0(x, y) + \mathrm{i}Q_0(x, y)$ of the complex variable $t = x + \mathrm{i}y$. For a simply connected planform domain Riemann's theorem (see Carrier, Krook & Pearson 1966) guarantees existence of an analytic function

$$t = M(\zeta), \tag{2.18}$$

representing a conformal mapping of the interior of the channel-planform domain on to the upper half of the auxiliary $\zeta = \xi + \mathrm{i}\eta$ complex plane. We select $M(\zeta)$ so that the far upstream and downstream (entrance and exit) sections are mapped on the points $\zeta = a_j$ $(j = 1, 2, \ldots)$ of the real ξ axis. In this plane $F_0[M(\zeta)] = f_0(\zeta)$ is readily obtained,

$$f_0(\zeta) = g_0(\xi, \eta) + \mathrm{i}q_0(\xi, \eta) = -\frac{1}{\pi}\sum_{j=1} C_j \ln\left(a_j - \zeta\right). \tag{2.19}$$

The solution of the leading-order outer problem is thus provided (in parametric representation) by the union of (2.18) and (2.19). In agreement with the general matching scheme of van Dyke (1975) we cannot at this stage formulate the problem governing the outer correction G_1. We thus turn now to address the 'inner' problem.

2.2. *The inner problem*

For a rectangular channel cross-section we employ the local orthogonal system of coordinates (s, n, z), where the s and n coordinate lines lie at the channel midplane and are parallel (in the local streamwise direction) and perpendicular (pointing into the fluid domain), respectively, to the sidewall (see figure 1*b*). The corresponding metric coefficients are $h_n = h_z = 1$ and $h_s = 1 + \kappa n$, where κ is the dimensionless (presumed $O(1)$) local curvature of the channel planform boundary. We expect that for $\varepsilon \to 0$ the flow adapts to no slip within a narrow layer adjacent to the sidewalls. We thus define an inner normal coordinate N via

$$n = \delta(\varepsilon)N, \tag{2.20}$$

where $\delta(\varepsilon) \to 0$ for $\varepsilon \to 0$ and $N \sim O(1)$ within the inner region. From the continuity equation in conjunction with the vanishing at the sidewall of u_n we anticipate that $u_n \sim O(\delta)$ within the inner domain and accordingly write $\boldsymbol{u}_\parallel = (U_s, \delta U_N)$ for the velocity field and denote by P the pressure there. Furthermore, by inspection of the s-equation of motion one readily concludes that the distinguished inner-limit process corresponds to selecting $\delta = \varepsilon$. To leading order we thus obtain the equations of motion

$$\frac{\partial P}{\partial s} \sim \frac{\partial^2 U_s}{\partial z^2} + \frac{\partial^2 U_s}{\partial N^2} \quad , \quad \frac{\partial P}{\partial N} = \frac{\partial P}{\partial z} \sim 0 \tag{2.21}$$

and the equation of continuity

$$\frac{\partial}{\partial s}(PU_s) + \frac{\partial}{\partial N}(PU_N) \sim 0. \tag{2.22}$$

For future reference we note that by (2.21) $P = P(s)$ is uniform across the inner domain and therefore equal to the local 'outer' pressure $p|_{n=0}$. With a view to subsequent asymptotic matching we present the inner velocity components

$$PU_s \sim -\frac{3}{2}\left(1-z^2\right)\left(\frac{\partial G_0}{\partial s} + \varepsilon\bar{c}\frac{\partial G_1}{\partial s}\right) + PV_s(s, N, z) + O(\varepsilon) \tag{2.23}$$

and

$$PU_N \sim -\frac{3}{2}\left(1-z^2\right)\left(\frac{1}{\varepsilon}\frac{\partial G_0}{\partial n} + \bar{c}\frac{\partial G_1}{\partial n}\right) + PV_N(s, N, z) + O(\varepsilon). \tag{2.24}$$

We note that since G_0 satisfies (2.14) together with the homogeneous Neumann condition (2.16) at the sidewall, $\partial G_0/\partial n \sim O(\varepsilon)$, within the inner domain. Thus, all of the terms explicitly appearing on the right-hand side of (2.24) are $O(1)$. Furthermore, as a matter of convenience we add in (2.23) the term $\varepsilon\bar{c}\partial G_1/\partial s$ (which is $O(\varepsilon)$) and use in the above the hybrid notation involving both (s, n) and (s, N). The first terms in (2.23) and (2.24) trivially satisfy the matching conditions in the intermediate domain characterized by the simultaneous limits $n \to 0$ and $N \to \infty$. The correction terms thus satisfy

$$V_s,\ V_N = 0 \quad \text{as} \quad N \to \infty. \tag{2.25}$$

To leading order the no-slip boundary conditions imposed on U_s and U_N yield

$$PV_s = \frac{3}{2}\left(1-z^2\right)\frac{\partial G_0}{\partial s} \tag{2.26}$$

and

$$PV_N = \frac{3}{2}\left(1-z^2\right)\left(\frac{1}{\varepsilon}\frac{\partial G_0}{\partial n} + \bar{c}\frac{\partial G_1}{\partial n}\right) \tag{2.27}$$

at the sidewalls $n, N = 0$ as well as at the channel top and bottom walls $z = \pm 1$. (For future reference we retain the first term on the right-hand side of (2.27), although by (2.16) it vanished at $n = 0$; see § 2.4.2.)

Substituting (2.23) into (2.21) we find that V_s is governed by

$$\frac{\partial^2 V_s}{\partial z^2} + \frac{\partial^2 V_s}{\partial N^2} = 0. \tag{2.28}$$

Inasmuch as to leading order G is uniform throughout the inner domain (for s fixed) we may write the solution of (2.28) satisfying (2.25) and (2.26) as

$$PV_s = \left(\frac{\partial G_0}{\partial s}\right)_{n=0} \bar{V}_s(N, z), \tag{2.29a}$$

where

$$\bar{V}_s = \frac{48}{\pi^3}\sum_{k=0}^{\infty}\frac{(-1)^k\,\mathrm{e}^{-N\left(\frac{\pi}{2}+k\pi\right)}}{(1+2k)^3}\cos\left[\left(\frac{\pi}{2}+k\pi\right)z\right]. \tag{2.29b}$$

Substituting (2.23) and (2.24) into the $O(1)$ equation of continuity (2.22) and recalling that both G_0 and G_1 are harmonic (2.14) we obtain

$$\frac{\partial}{\partial s}(PV_s)+\frac{\partial}{\partial N}(PV_N)=0. \tag{2.30}$$

We next integrate this equation over the entire inner domain (at a fixed s). Making use of (2.16), (2.25) and (2.27) we obtain

$$\bar{c}\left(\frac{\partial G_1}{\partial n}\right)_{n=0}=\int_0^{\infty}\int_0^1\frac{\partial}{\partial s}(PV_s)\,\mathrm{d}z\,\mathrm{d}N, \tag{2.31}$$

which by use of (2.29*a*) yields

$$\frac{\partial G_1}{\partial n}=\frac{\partial^2 G_0}{\partial s^2}\quad \text{at}\quad n=0 \tag{2.32}$$

and

$$\bar{c}=\int_0^{\infty}\int_0^1\bar{V}_s\,\mathrm{d}z\,\mathrm{d}N. \tag{2.33}$$

When substituting (2.29*b*) we obtain

$$\bar{c}=6\left(\frac{2}{\pi}\right)^5\sum_{k=0}^{\infty}(2k+1)^{-5}\approx 0.63 \tag{2.34}$$

(cf. Sharipov 1999). While (2.32) is apparently a purely outer-domain relation connecting G_1 and G_0, it actually reflects the outer limit of the mass flux normal to the sidewall associated with the $O(1)$ fluid motion within the inner domain. This is somewhat similar to the familiar 'displacement effect' in higher-order boundary-layer theory at high Reynolds numbers (Lighthill 1958).

Within the framework of the leading-order inner problem, V_N remains indeterminate. We recognize, however, that U_N actually represents $u_n=\varepsilon U_N$, i.e. an $O(\varepsilon)$ contribution to the velocity field within the inner domain. As such, it can be determined only after the calculation of the first-order outer correction, in accordance with van Dyke's general matching scheme referred to above. Furthermore, since the width of the inner domain is itself $O(\varepsilon)$, fluid-velocity correction there will only have an $O(\varepsilon^2)$ contribution to the total mass-flow rate through the channel. Thus, to complete an $O(\varepsilon)$ calculation of the mass-flow rate, it is sufficient to evaluate the correction G_1 in the outer domain, which we address next.

2.3. *The $O(\varepsilon)$ outer-domain correction*

The correction $G_1(x,y)$ is governed by a Neumann problem consisting of (2.14) in conjunction with (2.32) at the sidewalls. To complete the problem statement we need to stipulate conditions at the entrance and exit sections. As elaborated on in the next section, it is more convenient to formulate the problem when the mass-flow rates (rather than pressures) are specified in these sections. The requisite condition on $\partial G_1/\partial n$ is thus determined so as to compensate for the deficit of the mass-flow rate associated with the (relatively slow) flow within the inner domains adjacent to the sidewalls. Similar to the derivation of (2.32), integration of V_S over the entire inner domain yields the total deficit $2\varepsilon\bar{c}\partial G_0/\partial n$ at the (presumed uniform) semi-infinite entrance and exit channels. Making use of (2.17) we thus obtain the condition

$$\frac{\partial G_1}{\partial n}=2\frac{\partial G_0}{\partial n}\quad (j=1,2,\ldots). \tag{2.35}$$

Similarly to the above calculation of G_0 we apply (2.18) mapping the (presumed simply connected) channel planform on to the upper half of the $\zeta = \xi + \mathrm{i}\eta$ plane. Making use of the conformal nature of the transformation by means of the analytic function $M(\zeta)$, we express the derivatives of G_0 and G_1 appearing in (2.32) in terms of their ζ-plane counterparts $g_0 = \mathrm{Re}\{f_0\}$ and g_1, respectively (where Re{} denotes the real part of a complex-valued expression). Thus, since the sidewalls are mapped on the real ξ axis

$$\left(\frac{\partial G_1}{\partial n}\right)_{n=0} = \frac{1}{|M'|}\left(\frac{\partial g_1}{\partial \eta}\right)_{\eta=0}. \tag{2.36}$$

Similarly, an elementary displacement in the downstream direction along the wall ds corresponds to an increment dξ; hence

$$\left(\frac{\partial^2 G_0}{\partial s^2}\right)_{n=0} = \frac{1}{|M'|}\frac{\partial}{\partial \xi}\left(\frac{1}{|M'|}\mathrm{Re}\{f_0'\}\right)_{\eta=0}, \tag{2.37}$$

where the primes denote differentiation with respect to ζ. Substituting these expressions into (2.32) we obtain

$$\frac{\partial g_1}{\partial \eta} = \frac{\partial}{\partial \xi}\left(\frac{1}{|M'|}\mathrm{Re}\{f_0'\}\right) \quad \text{at} \quad \eta = 0. \tag{2.38}$$

Employing the Green's function for the Neumann problem in the half-plane (cf. Polyanin 2002) we get

$$g_1 = \frac{2}{\pi}\left\{\frac{1}{4}\int_{-\infty}^{\infty}\frac{\partial}{\partial \beta}\left[\frac{f_0'(\beta)}{|M'(\beta)|}\right]\ln\left[(\xi-\beta)^2+\eta^2\right]\mathrm{d}\beta - \sum_j \frac{C_j}{W_j}\ln\left(|\zeta - a_j|\right)\right\}, \tag{2.39}$$

which represents a superposition of the effects of (2.35) at the entrance and exit sections and (2.32) along the channel sidewalls.

2.4. *Extensions of the basic model*

The foregoing analysis is readily adapted to incompressible flows of homogeneous fluids ($\rho = 1$). Since (2.6)–(2.8) remain the same we still obtain (2.10). Relation (2.12) for the mass-flow rate still holds provided that we modify the definition of G to read

$$G = \frac{1}{3}p. \tag{2.40}$$

In terms of this modified definition the rest of the analysis follows as before when throughout §2.2 PU_N, PU_s, PV_N and PV_s are replaced by U_N, U_S, V_N and V_S, respectively.

2.4.1. *Weak rarefaction effects*

In shallow micro-configurations, fluid motion takes place within the narrow (≈ 1 μm) gap between parallel plates (Arkilic *et al.* 1997; Lee *et al.* 2001, 2002*a*,*b*; Yu *et al.* 2005). Adopting the quantitative definition

$$Kn = \frac{\mu}{2H\tilde{p}}\left(\frac{\pi R\tilde{T}}{2}\right)^{1/2}, \tag{2.41}$$

expressing the ratio of the molecular mean-free path and channel depth in terms of macroscopically measurable physical quantities, one finds for air at standard atmospheric conditions $Kn \approx 10^{-2}$–10^{-1} (Beskok, Karniadakis & Trimmer 1996;

Ho & Tai 1998; Jang & Wereley 2004). Focusing on the range $Kn < 0.1$ gas motion is usually described by means of a continuum slip-flow model consisting of the hydrodynamic (Navier–Stokes–Fourier) equations which at solid walls are supplemented by appropriate velocity-slip and temperature-jump conditions (Gad-El-Hak 1999; Cercignani 2000; Sone 2002). In the absence of temperature gradients, the condition $\boldsymbol{u}_{\parallel} = 0$ is thus replaced by the Navier-type conditions

$$\boldsymbol{u}_{\parallel} = \mp \sigma Kn \frac{\partial \boldsymbol{u}_{\parallel}}{\partial z} \quad \text{at} \quad z = \pm 1. \tag{2.42}$$

In (2.42) σ is the viscous slip coefficient representing the interaction between gas molecules and solid walls. In subsequent illustrations we employ the value $\sigma = 1.1466$ obtained by Albertoni, Cercignani & Gotusso (1963) through the solution of the Kramers problem, assuming purely diffuse molecular reflection at the wall. (The relation between σ and the momentum accommodation coefficient has been studied by Sharipov 2003; see also Ewart *et al.* 2007.) Since $\mu = \mu(T)$, by (2.41) under isothermal conditions $Kn = Kn_0/p$, where Kn_0 corresponds to the reference conditions. When making use of (2.42) one obtains (we note here a typographical error in the sign of the second term on the right-hand sides of (3.1) and (3.2) in Gat *et al.* 2008)

$$\boldsymbol{u}_{\parallel} = -\left[\frac{1}{2}\left(1 - z^2\right) + \sigma \frac{Kn_0}{p}\right] \nabla_{\parallel} p \tag{2.43}$$

instead of (2.10) (cf. Arkilic *et al.* 1997; Sharipov & Seleznev 1998, for the one-dimensional counterpart). Substituting (2.43) into (2.5) and integrating in conjunction with the requirement $w = 0$ at $z = \pm 1$ lead to (2.14) where the definition of (2.11) is now replaced by

$$G = \frac{1}{6} p^2 + \sigma Kn_0 p. \tag{2.44}$$

Furthermore, for the z-velocity component we obtain

$$w = \frac{1}{4} z \left(1 - z^2\right) \frac{1}{p} \nabla_{\parallel}^2 \left(\frac{1}{3} p^2\right) \tag{2.45}$$

which, in general, does not vanish when $Kn \neq 0$ (cf. Arkilic *et al.* 1997). With the redefinition of G, the rest of the analysis of the leading-order outer problem remains intact. Imposing the slip conditions at the sidewalls involves a tedious calculation. To avoid this we continue to impose there the no-slip conditions which, in turn, introduce an $O(Kn)$ error into the resulting inner flow field and an $O(\varepsilon Kn)$ in the outer correction as well in the calculation of integral quantities. Thus, subsequent results for the total mass-flow rate and viscous resistance of the channel remain unchanged at non-zero $Kn \ll 1$ when expressed in terms of the modified definition of G (2.44).

2.4.2. *Non-rectangular cross-sections*

The application of different micro-fabrication technologies results in a variety of cross-sectional shapes as illustrated in figure 7 in the Appendix. Thus, for instance, trapezoidal cross-sections (figure 7*a*) are produced by means of photolithography (Wu & Cheng 2003; Wu, Wu & Wei 2009), whereas some etching methods (MacInnes, Du & Allen 2003) yield quarter-circular sidewalls (as in figure 7*c*). To consider the effects of the specific shape of the channel sidewalls we employ a local orthogonal system of coordinates (s, n, z) similar to that defined in § 2.2. Unlike a rectangular cross-section, where the sidewall simply corresponds to $N = 0$, here its local (at a fixed s) geometry

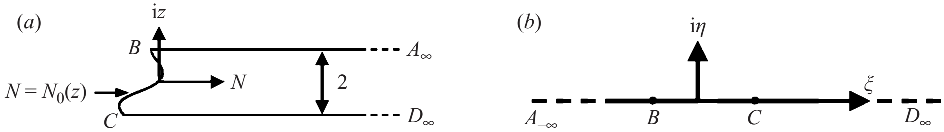

FIGURE 2. A schematic view and coordinates definition for the inner domain in (*a*) the $N + \mathrm{i}z$ physical plane and (*b*) the auxiliary $\xi + \mathrm{i}\eta$ plane.

is defined by $N = N_0(z)$ (see figure 2*a*). The statement of the inner problem stays the same as in the above (2.20)–(2.28).

Unlike the above derivation of the matching condition on $\partial G_1/\partial n$ for a rectangular cross-section the first term on the right-hand side of (2.27) does not vanish at $N = N_0(z)$. Taylor series expansion of this term in conjunction with (2.14) and definition (2.20) yield

$$PV_N \sim -\frac{3}{2}\left(1-z^2\right)\left[N_0(z)\left(\frac{\partial^2 G_0}{\partial s^2}\right)_{n=0} - \bar{c}\left(\frac{\partial G_1}{\partial n}\right)_{n=0}\right] \quad \text{at } N = N_0(z). \tag{2.46}$$

Integration of (2.30) over the entire inner domain for a fixed s in conjunction with the matching conditions (2.25) and representation (2.29*a*) of V_s yield

$$\left(\frac{\partial^2 G_0}{\partial s^2}\right)\int_{N_0(z)}^{\infty}\int_{-1}^{1}\bar{V}_s(N,z)\,\mathrm{d}z\,\mathrm{d}N - \int_{-1}^{1}(PV_N)_{N_0(z)}\,\mathrm{d}z = 0. \tag{2.47}$$

Substituting (2.46) we obtain (2.32) and

$$\bar{c} = \bar{c}_1 + \bar{c}_2, \tag{2.48}$$

where

$$\bar{c}_1 = \frac{1}{2}\int_{N_0(z)}^{\infty}\int_{-1}^{1}\bar{V}_s(N,z)\,\mathrm{d}z\,\mathrm{d}N \tag{2.49a}$$

and

$$\bar{c}_2 = \frac{3}{4}\int_{-1}^{1}(1-z^2)N_0(z)\,\mathrm{d}z. \tag{2.49b}$$

The former contribution (2.49*a*) is a straightforward generalization of (2.33). Thus (cf. § 2.3) it represents the mass-flow-rate deficit as a result of the slowing down of the flow adjacent to the sidewalls. To evaluate $\bar{c}_1$ we need to obtain the velocity perturbation V_s satisfying the Dirichlet problem consisting of (2.25), (2.26) and (2.28) within the inner domain (figure 2*a*). Closed-form analytic expressions for $\bar{c}_1$ are obtained in the Appendix via application of conformal mapping. The latter term (2.49*b*) represents a purely 'geometric' effect – the diminution of the mass-flow rate associated with G_0 owing to the replacement of a rectangular cross-section (whose sidewall is located at $N = 0$) by the actual cross-section (whose sidewall is at $N_0(z)$). We thus conclude that the effects of the sidewall geometry – both 'direct' (affecting fluid motion within the inner domain) and 'indirect' (affecting G_1 within the outer domain) – are embodied in the specific numerical value that the coefficient $\bar{c}$ assumes. The calculation of $\bar{c}$ for various cross-sections is illustrated in the Appendix.

3. Sidewall effects on the viscous resistance of straight and uniform channels

Exact analytic and numerical solutions exist for fully developed flows through straight and uniform channels. Comparison with these allows us to verify the improved accuracy achieved through the incorporation into the present analysis of sidewall effect. To this end we focus in the following on the various approximations for the mass-flow rate through the channel.

For a straight and uniform channel $\nabla_{\|} G$ is uniform. Making use of (2.12) and neglecting sidewall effects, we readily obtain the dimensionless mass-flow rate (normalized by $2\rho_0 p_0 H^3/\mu$)

$$\dot{m}_0 = \frac{\Delta G}{L}, \tag{3.1}$$

where ΔG denotes the drop in G along a channel segment of length L. Since $\nabla_{\|} G_0$ is uniform the matching condition (2.32) reduces to a homogeneous Neumann condition on G_1 at the sidewalls. Both G_1 and G_0 thus satisfy similar Neumann problems, and hence G_1 is proportional to G_0. To maintain a prescribed mass-flow rate we need to compensate for losses within the inner domain through multiplying $\nabla_{\|} G$ by the factor $1 + 2\varepsilon\bar{c}$ (cf. (2.15) and (2.35)). Thus, to account for the leading $O(\varepsilon)$ correction of the sidewalls, we need to modify (3.1) to

$$\dot{m}_1 = (1 + 2\varepsilon\bar{c})^{-1} \frac{\Delta G}{L}. \tag{3.2}$$

The above scheme in which the conditions at the entrance and exit sections are determined so as to maintain a prescribed value of $\dot{m}$ results in the formulation of a Neumann problem governing G_1 (which is independent of the actual length of the ‘semi-infinite’ entrance and exit channels). Alternatively, one could in principle consider the entrance and exit pressures and hence ΔG prescribed and calculate the reduction in $\dot{m}$ associated with the sidewall effects. This approach will result in G_1 being governed by a ‘mixed’ problem involving homogeneous Dirichlet-type conditions at the entrance and exit sections. For the particular case of a uniform channel both schemes are equally straightforward. In the latter scheme we obtain the reduction in the mass-flow rate associated with the direct effect on the flow within the inner domains adjacent to the sidewalls $-2\varepsilon\bar{c}\Delta G/L$; hence

$$\dot{m}_1^* = (1 - 2\varepsilon\bar{c}) \frac{\Delta G}{L} \tag{3.3}$$

which, within $O(\varepsilon)$, is equivalent to (3.2).

Figure 3 describes the variation with ε of $R_{\dot{m}}$, the ratios between the various approximations of the mass-flow rate $\dot{m}_0$ (dashed line), $\dot{m}_1$ (solid line) and $\dot{m}_1^*$ (dash-dotted line) and the corresponding exact analytic or numerical solution, respectively. Thus, the deviation from $R_{\dot{m}} = 1$ is the relative error associated with the asymptotic calculation. Experimental data for the mass-flow rate normalized by the same theoretical solution are included to complement the picture.

Figure 3(*a*) is concerned with uniform rectangular channels. Here D is equal to half of the channel width so that $\varepsilon = 1$ corresponds to a square cross-section. As a matter of convenience normalization is here based on explicit analytic (series-form) expressions of Jang & Wereley (2004) for compressible slip flows at small Knudsen numbers. We have selected $Kn = 0.05$ as a typical reference value corresponding by (2.41) to standard atmospheric conditions at the channel exit. The corresponding results from the combined analytic and numerical calculations of Sharipov (1999) (solid triangles) and Aubert & Colin (2001) (solid squares) nearly coincide with $R_{\dot{m}} = 1$. Also indicated are the experimental data of Zohar *et al.* (2002) (+) and Ewart *et al.* (2007) (×). In the absence of experimental data for gas flows through channels of larger ε we have added the results of Akbari *et al.* (2009) (circles) for liquid flows through rectangular

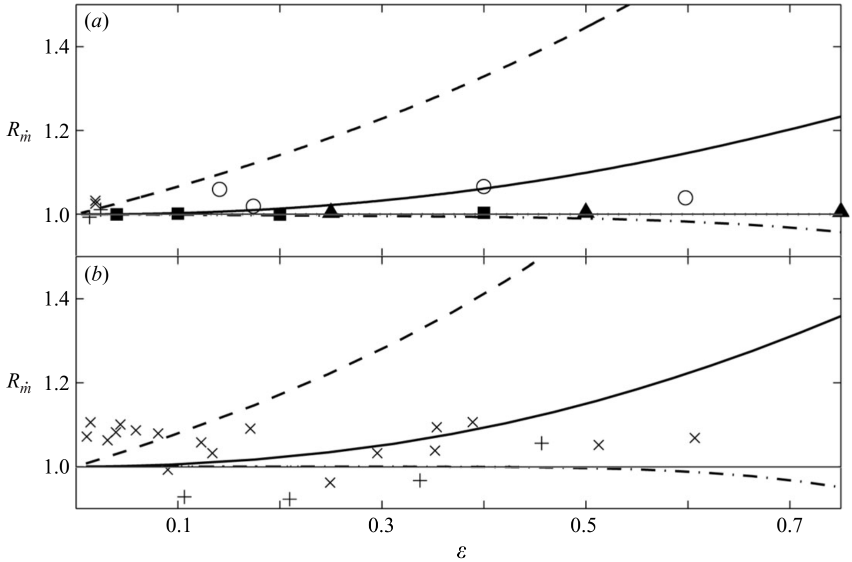

FIGURE 3. Variation with ε of the normalized mass-flow rate according to $\dot m_0$ (dashed line), $\dot m_1$ (solid line) and $\dot m_1^*$ (dash-dotted line). (*a*) Gas slip flow through uniform rectangular channels ($Kn = 0.05$ at the exit section). Calculations of Sharipov (1999) are denoted by ▲ and those of Aubert & Colin (2001) by ■. Experimental data of Zohar *et al.* (2002) are denoted by + and those of Ewart *et al.* (2007) by ×. All these are normalized by reference to Jang & Wereley (2004). Experimental data of Akbari, Sinton & Bahrami (2009) (○) for liquid flow are normalized by exact incompressible solution. (*b*) Liquid flow through uniform trapezoidal ($\gamma = 54.7^0$; see figure 7) channels; normalization by reference to Morini (2004); experimental results by Wu & Cheng (2003) (×) and Wu *et al.* (2009) (+).

channels, which are normalized by the corresponding exact solution for incompressible flow (cf. White 1986). Figure 3(*b*) considers the (normalized) mass-flow rate through a straight channel with a uniform isosceles trapezoidal cross-section characterized by $\gamma = 54.7^0$ (see figure 7*a*). For this cross-section $\bar c \approx 0.73$ (see the Appendix and figure 8) in (3.2) and (3.3). The above theoretical approximation and the experimental data of Wu & Cheng (2003) (×) and Wu *et al.* (2009) (+) are here normalized by the simulation results of Morini (2004).

As expected, in both parts of the figure the relative error associated with $\dot m_0$ initially grows linearly with ε (and subsequently at a faster rate). Thus, already at relatively small ε, $\dot m_0$ no longer qualifies as a quantitative approximation of the actual mass-flow rate. The results based on $\dot m_1$ (3.2) represent a substantial improvement. Thus, in marked contrast with $\dot m_0$, up to $\varepsilon \approx 0.4$, $\dot m_1$ involves an error of less than ≈10 %. In both parts of the figure $\dot m_1^*$ is remarkably accurate being nearly indistinguishable from the exact reference up to $\varepsilon \approx 0.5$. It is thus interesting to consider the difference between $\dot m_1^*$ and $\dot m_1$. While both are equivalent to $O(\varepsilon)$ they differ at $O(\varepsilon^2)$; from (3.2) and (3.3), $\dot m_1^*/\dot m_1 = 1 - (2\varepsilon\bar c)^2$. The variation may be traced back to the difference between the respective schemes. As mentioned above, in the calculation leading to (3.2) we increase ΔG so as to ensure that the mass-flow rate is equal to that prescribed up to $O(\varepsilon)$. The correction G_1 thus obtained introduces an $O(\varepsilon^2)$ error (contributed by both the $O(\varepsilon)$ terms within the inner domain and the $O(\varepsilon^2)$ outer correction) which is not accounted for. In evaluating $\dot m_1^*$ we keep ΔG as prescribed and directly calculate the reduction of the mass-flow rate resulting from the sidewalls. Figure 3

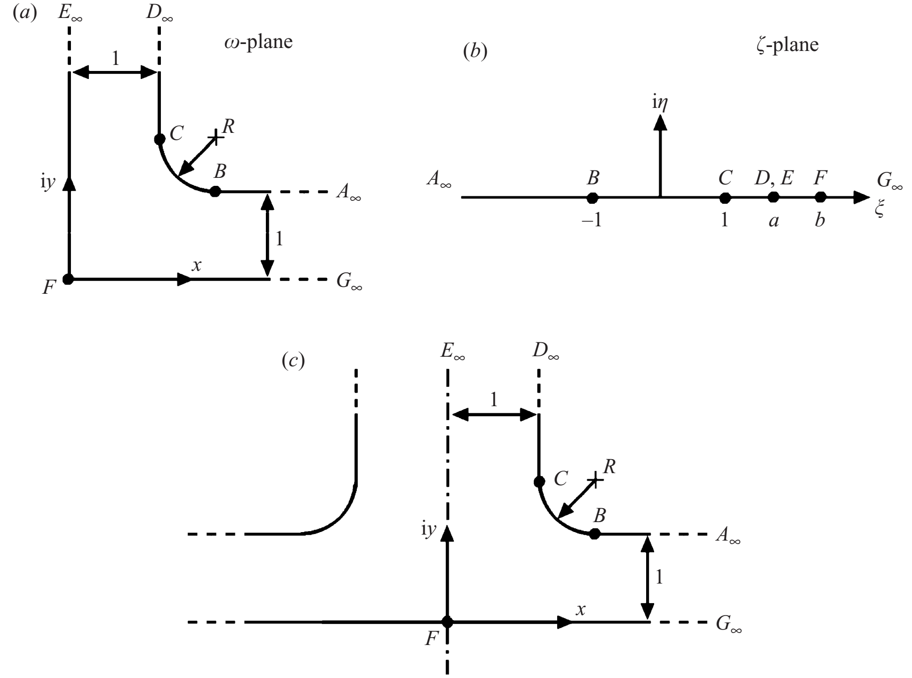

FIGURE 4. A schematic view of (*a*) the corresponding picture in physical $x + iy$ plane and (*b*) the 90° bend in auxiliary $\xi + i\eta$ plane and (*c*) of the symmetric T-junction.

indicates that the latter approach may be preferable. It is, however, not readily applicable to non-uniform channels. In these configurations (addressed in the next section) we rely on $\dot{m}_1$ (3.2) which, as demonstrated above, provides a substantially improved accuracy relative to $\dot{m}_0$, thereby significantly extending the range of ε where a quantitative approximation is obtained.

The experimental data presented show no definite trend with increasing ε. This seems appropriate given that such trends are already embodied in the exact theoretical solutions normalizing these data. Furthermore, according to the various sources there is a large scatter in the experimental measurements (±6 % according to Zohar *et al.* 2002, ±10 % as reported by Akbari *et al.* 2009 and ±11 % documented by Wu & Cheng 2003). Thus, contrary to the superficial appearance (enhanced by our selection of normalization and large scale and the present omission of ‘error bars’; cf. figure 3 of Morini 2004) our calculations (together with the exact reference solutions) do fall within the margins of error of the empirical data.

4. The flow through non-uniform shallow configurations

To illustrate the effects of the sidewalls on the viscous resistance for configurations other than the uniform straight channel we consider the 90° turn whose planform is defined in figure 4(*a*). The transformation (Kober 1957)

$$M(\zeta) = \frac{1}{\pi}\left[1 + \left(\frac{b+1}{b-1}\right)^{1/2}\right]^{-1} \int_0^{\zeta} \left[\frac{(b+1)^{1/2}(\zeta_1 - 1)^{1/2} + (b-1)^{1/2}(\zeta_1 + 1)^{1/2}}{(b-1)^{1/2}(\zeta_1 - a)(\zeta_1 - b)^{1/2}}\right] \mathrm{d}\zeta_1 \tag{4.1}$$

maps the interior of the channel in the physical $t = x + \mathrm{i}y$ plane on to the upper half of the auxiliary $\zeta = \xi + \mathrm{i}\eta$ plane as depicted in figure 4(*b*). The parameters a, b appearing in (4.1) are determined so that the radius of the arc BC is

$$R = \mathrm{Im}\{M(1) - M(-1)\}, \tag{4.2}$$

where Im{} denotes the imaginary part of a complex-valued expression, and also so that the semi-infinite channels are of width unity which, by principal-value integration along a small semicircle centred at $\zeta = a$, yields the equation

$$\left[1 + \left(\frac{b+1}{b-1}\right)^{1/2}\right]^{-1} \left[\left(\frac{a+1}{b-a}\right)^{1/2} + \left(\frac{b+1}{b-1}\right)^{1/2} \left(\frac{a-1}{b-a}\right)^{1/2}\right] = 1. \tag{4.3}$$

The leading-order outer solution is obtained from (2.19). Substituting into (2.39) we then get g_1; hence

$$\begin{aligned} g \sim g_0 + \varepsilon\bar{c}g_1 = {} & \frac{1}{\pi}(1 + 2\varepsilon\bar{c}) \ln\left|\frac{\zeta - a}{b - a}\right| \\ & - \frac{\varepsilon\bar{c}}{2\pi} \int_{-\infty}^{\infty} \frac{\partial}{\partial\beta}\left[\frac{1}{|M'(\beta)|}\frac{1}{\pi(\beta - a)}\right] \ln\left[(\xi - \beta)^2 + \eta^2\right] \mathrm{d}\beta. \end{aligned} \tag{4.4}$$

Far upstream and downstream of the turn (i.e. when $\zeta \to \infty, a$, respectively; cf. figure 4*a*) the effect of the bend attenuates and, by (2.17) and (2.35), $\nabla_{\parallel} G$ becomes uniform across the channel. The flow then becomes identical to the flow through a uniform straight channel. Consequently, the difference between ΔG required to drive a unit (dimensionless) mass-flow rate through the actual bend configuration and $\Delta G^{(0)}$, the requisite value for a corresponding straight and uniform channel, approaches a finite limit with increasing channel length. There is some arbitrariness in specifying the reference uniform channel. We here select for comparison the pair of semi-infinite channels extending from $x = 1$ to $x \to \infty$ and from $y = 1$ to $y \to \infty$, respectively. Making use of (3.2) for $\dot{m} = 1$, the vanishing of G at the origin and the upstream–downstream symmetry of the bend, we write the limit of the difference $\Delta G - \Delta G^{(0)}$:

$$\Delta = 2 \lim_{x\to\infty} [G(x, y) - (x - 1)(1 + 2\varepsilon\bar{c})] = 2 \lim_{\zeta\to\infty} [g(\zeta) - (m(\zeta) - 1)(1 + 2\varepsilon\bar{c})]. \tag{4.5}$$

When substituting (4.1) and (4.4) we obtain

$$\Delta \sim \Delta_0 + \bar{c}\varepsilon\Delta_1, \tag{4.6a}$$

where

$$\Delta_0 = \lim_{\zeta\to\infty} 2\,[g_0(\zeta) - (M(\zeta) - 1)] \tag{4.6b}$$

and

$$\Delta_1 = \lim_{\zeta\to\infty} 2\,[g_1(\zeta) - 2(M(\zeta) - 1)]. \tag{4.6c}$$

This representation of Δ is useful in that it separates the effects of the channel planform embodied in Δ_0 and Δ_1 from those associated with ε and the shape of the sidewalls ($\bar{c}$), respectively. For a unit mass-flow rate through a uniform-channel segment of total length $2L$, (3.2) yields $\Delta G^{(0)} = 2(1 + 2\varepsilon\bar{c})L$. Furthermore, provided that L is sufficiently large so that $\nabla_{\parallel} G$ is already approximately uniform across both channel sections at $x = L + 1$ and $y = L + 1$, respectively, we may use the above to obtain

$$\Delta G \sim 2(1+2\varepsilon\bar{c})L+\Delta. \tag{4.7}$$

We thus recognize Δ as the present normalized counterpart of the 'equivalent length' prevailing in the literature concerning viscous (incompressible) flows through pipe systems. Thus, pressure-head losses associated with bends, valves or constrictions are quantified in terms of an additional length of a straight and uniform conduit (White 1986). Alternatively, by the linearity of ΔG and $\dot{m}$, we may modify (3.2) to

$$\dot{m}=\frac{\Delta G}{2(1+2\varepsilon\bar{c})L+\Delta}, \tag{4.8}$$

where now Δ represents the reduction of the mass-flow rate at a given ΔG.

The forgoing calculation for the flow through the 90° turn is readily adapted to describe the symmetric T-junction appearing in figure 4(*c*). The line $E_\infty F$ is now a reflection-symmetry line (rather than a solid wall) where $\partial G/\partial n = 0$. The calculation of G_0 remains the same as before (since G_0 originally satisfies a homogeneous Neumann condition along $E_\infty F$). The modification of the $O(\varepsilon)$ correction to G involves two elements. The $(2\varepsilon\bar{c})$ term in the factor pre-multiplying the first (logarithmic) term on the right-hand side of (4.4) represents the compensation for the mass-flow-rate deficit associated with the sidewalls at the far downstream section $D_\infty E_\infty$ (cf. the discussion preceding (2.35)). Since, this effect results now from the presence of only a single wall, this term is accordingly replaced by $\varepsilon\bar{c}$. The integral term on the right-hand side represents the contribution of $\partial G_1/\partial n$ along the channel sidewalls, as obtained from (2.31). To subtract the contribution of the now non-existent wall $E_\infty F$ we need to eliminate the interval (a, b) from this integral. The expressions for Δ_1 (4.6) and $\dot{m}$ (4.8) are accordingly modified to

$$\Delta_1=\lim_{\zeta\to\infty}\left[g_1(\zeta)-2(M(\zeta)-1)\right]-\lim_{\zeta\to a}\left[g_1(\zeta)-(\operatorname{Im}\{M(\zeta)\}-1)\right] \tag{4.9}$$

and

$$\dot{m}=\frac{\Delta G}{2(1+\frac{3}{2}\varepsilon\bar{c})L+\Delta}. \tag{4.10}$$

The above analysis identifies Δ, the equivalent length appearing in (4.7), (4.8) and (4.10), as the single parameter characterizing the viscous resistance of the shallow configuration. Figure 5 presents the variation with the radius R (see figure 4*a,c*) of Δ_0 (4.6*b*) and Δ_1 (4.6*c*) or (4.9) comprising Δ for a 90° turn and a symmetric T-junction, respectively. As could be anticipated, Δ_0 is diminishing with increasing R (which effectively increases the local cross-sectional area). The relative changes in Δ_1 are smaller; Δ_1 for the turn grows monotonically with R, whereas that for the T-junction is initially diminishing, passes through a shallow minimum for $R \approx 0.67$ and then becomes monotonically increasing.

Figure 6 describes the effects of various parameters on the deviation of the asymptotic calculations (4.8) and (4.10) from the 'exact' values of $\dot{m}$ obtained through use of the finite-element COMSOL 3.4 package. To this end we present the variation of $R_{\dot{m}}$, the ratio of the corresponding asymptotic and 'exact' values (i.e. $R_{\dot{m}} = 1$ represents an 'exact' calculation). We here focus on finite ($L = 1.5$) 90° bend and symmetric T-junction configurations (cf. figure 4*a,c*) with rectangular cross-sections. (Calculations based on the above analysis as well as the numerical simulations demonstrate that already for $L \approx 1$, G becomes nearly uniform across both the

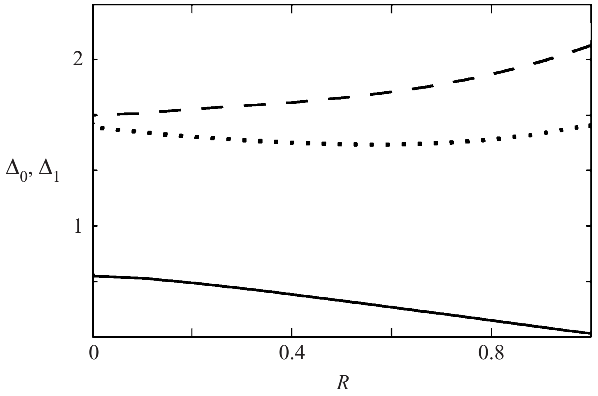

FIGURE 5. Dependence on R of the contributions to Δ: Δ_0 (solid line) and Δ_1 for the 90° turn (dashed line) and for the symmetric T-junction (dotted line), respectively.

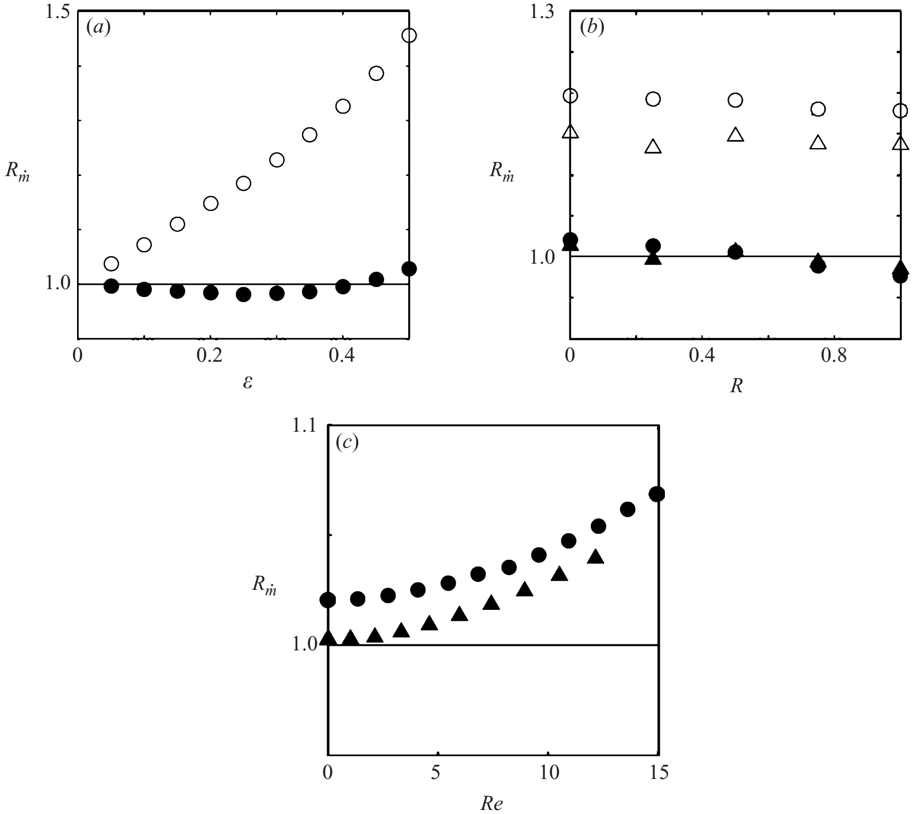

FIGURE 6. The ratio $R_{\dot m}$ of the asy mptotic and the finite-element calculations of the mass-flow rate through finite ($L = 1.5$) configurations. (a) Variation of $R_{\dot m}$ with ε for a 90° turn ($R = 1$) according to leading- and first-order calculations (hollow and solid circles, respectively). (b) Variation of $R_{\dot m}$ with R, the sidewall radius of curvature (see figure 4), for a 90° turn (circles) and a symmetric T-junction (triangles). Leading- and first-order calculations are marked by hollow and solid symbols, respectively; $\varepsilon = 0.125$. (c) Variation of $R_{\dot m}$ with Re for the 90° turn and $\varepsilon = 0.05$ (triangles) and 0.125 (circles).

entrance and exit sections, which supports our use of (4.8) and (4.10) for finite-length configurations.)

Figure 6(a) presents the variaton of $R_{\dot{m}}$ with ε for a 90° turn (figure 4a) characterized by $R = 1$. In the numerical simulation we have selected standard atmospheric exit conditions. Entrance pressures have been varied with ε so as to maintain $Re \approx 0.1$ at the channel exit. Similar to figure 3, the relative error associated with a leading-order calculation (hollow circles) grows initially linearly with ε. Thus, already at relatively small ε, this calculation ceases to provide a quantitative approximation. The incorporation of the sidewall effects in the first-order calculation (solid circles) results in a remarkably improved accuracy reflecting the nonlinear and non-monotonical variation of $R_{\dot{m}}$ with ε. Figure 6(b) presents values of $R_{\dot{m}}$ for bends (circles) and junctions (triangles) for $\varepsilon = 0.125$ and several values of the sidewall radius of curvature within the interval $0 \leqslant R \leqslant 1$. Similar to figure 6($a$), a substantial improvement of accuracy is achieved when replacing the leading order by an $O(\varepsilon)$ calculation of $\dot{m}$ (hollow and solid symbols, respectively). Furthermore, the values of $R_{\dot{m}}$ seem essentially independent of R, including $R \to 0$. This suggests that corners in the channel planform have only local effects on the flow field. Thus, while the formulation of the inner problem in § 2.2 has assumed $\kappa \sim O(1)$, the results concerning integral quantities seem nevertheless applicable to planform configurations involving corners.

The error introduced by the neglected fluid-inertial effects is examined in figure 6(c) which presents the variation of $R_{\dot{m}}$ (based on the $O(\varepsilon)$ calculation of $\dot{m}$) with Re for a finite ($L = 1.5$) 90° turn and $\varepsilon = 0.05$ (triangles) and 0.125 (circles). We see that $R_{\dot{m}} > 1$; i.e. the analysis neglecting inertial effects underestimates the actual viscous resistance of the configuration. As could be anticipated, the error is monotonically increasing with Re. However, even at a Reynolds number as large as $Re \approx 10$, the error introduced by the asymptotic approximation is still less that 5 % (for the larger value of $\varepsilon = 0.125$). It is worthwhile to note that the relative error introduced by the neglect of inertial effects is actually larger for the smaller values of ε. This reflects the fact that the errors involved in the present analysis (cf. (2.6)–(2.8)) are $O(\varepsilon^2)$ and $O(\varepsilon Re)$, respectively. Thus, at a given Re the latter becomes relatively more important with diminishing ε.

5. Concluding remarks

The present contribution is concerned with the classic Hele-Shaw problem of the flow through the narrow gap between parallel surfaces. Specifically, we have generalized the Hele-Shaw approximation to incorporate the no-slip condition at the configuration sidewalls with the goal of reducing the error involved in the calculation of the configuration viscous resistance from linear to quadratic in ε. This has required an extension of the asymptotic scheme including the construction of an ‘inner’ solution in the vicinity of the sidewalls, a first-order ‘outer’ correction and the asymptotic matching of the two in the resulting singular problem. The results presented in figures 3 and 6(a) unequivocally demonstrate that the above goal has been met. A remarkably improved accuracy has been achieved through the incorporation of sidewall effects. This substantially extends the range of ε for which the Hele-Shaw analysis provides a quantitative approximation.

Our present scheme reduces the viscous compressible (or incompressible) flow problem to a pair of Neumann problems within the two-dimensional planform domain. For a given configuration planform these problems need to be solved only once. Subsequently, one may readily obtain solutions for arbitrary (within the domain of validity) cross-sectional geometry, entrance and exit conditions and ε. The present analysis thus presents a viable alternative allowing for the rapid estimate of the performance of shallow micro-configurations. This is particularly true (but not limited to) geometries where appropriate conformal transformations are available (which then provide closed-form solutions). The present contribution has focused on the development of the general asymptotic scheme. The specific illustrations considered here have been selected so as to serve this purpose (e.g. to demonstrate the improved accuracy). Applications of the scheme to engineering problems (e.g. optimization of micro-channel networks) are currently being studied and will be reported elsewhere.

Appendix. Calculation of the coefficient $\bar{c}$ characterizing non-rectangular cross-sections

For a specific $N_0(z)$ the calculation of $\bar{c}_2$ (2.49*b*) is straightforward. The evaluation of $\bar{c}_1$ requires the calculation of V_s. To this end we map the inner domain within the $T = N + \mathrm{i}z$ plane (figure 2*b*) on to the upper half of the auxiliary $\zeta = \xi + \mathrm{i}\eta$ plane by means of analytic function $T = m(\zeta)$. In the ζ plane the harmonic function $v_S(\xi, \eta) = V_S(N, z)$ satisfies the transformed condition (2.26), namely

$$v_s = \frac{1}{2}\frac{\partial P}{\partial s}\left\{1 - \left(\mathrm{Im}\{m(\beta)\}\right)^2\right\} \quad \text{at} \quad \eta = 0. \tag{A1}$$

By use of the Green's function for the Dirichlet problem in the upper half-plane we obtain v_s. The corresponding $\bar{v}_s$ (cf. (2.29*a*)) is

$$\bar{v}_s = \frac{3}{2\pi}\int_{-\infty}^{\infty} \frac{\{1 - (\mathrm{Im}[m(\beta)])^2\}\eta \, \mathrm{d}\beta}{(\xi - \beta)^2 + \eta^2}, \tag{A2}$$

and $\bar{c}_1$ is accordingly

$$\bar{c}_1 = \frac{1}{2}\int_{-\infty}^{\infty}\int_{0}^{\infty} \bar{v}_s(\xi, \eta)\left|\frac{\mathrm{d}m}{\mathrm{d}z}\right|^2 \mathrm{d}\eta \, \mathrm{d}\xi. \tag{A3}$$

For polygonal cross-sectional shapes the requisite analytic function $m(\zeta)$ appearing in (A1) and (A2) may be obtained through application of the Schwarz–Christoffel transformation (Milne-Thomson 1968). Thus, for the trapezoidal cross-section (figure 7*a*) whose upper and lower vertices are mapped on $\zeta = -1$ and $\zeta = 0$, respectively, we obtain

$$m = \frac{2}{\pi}\zeta^{\frac{\gamma}{\pi}-1}(\zeta + 1)^{-\frac{\gamma}{\pi}}, \tag{A4}$$

and for a hexagonal shape (figure 7*b*) whose vertices are mapped on $\zeta = 0$ and $\zeta = \pm 1$, we obtain

$$m = \frac{2}{\pi}\zeta^{\frac{2\gamma}{\pi}-1}(\zeta - 1)^{-\frac{\gamma}{\pi}} \cdot (\zeta + 1)^{-\frac{\gamma}{\pi}}. \tag{A5}$$

(Since the dimensions within the inner domain are scaled by H, the dimensionless depths of both channels are equal to 2.) The values of $\bar{c}$ obtained via substitution of (A4) and (A5) in (A3) are depicted in figure 8 by the solid and dashed curves, respectively. At $\gamma = \pi/2$ both cross-sections become rectangular and accordingly $\bar{c} \approx 0.63$ for both of them. Also presented in figure 8 (by the horizontal dotted and dashed-dotted lines) are the values of $\bar{c}$ for the semicircular and quarter-circular sidewalls, respectively (see figure 7*c*,*d*). In these cases $\bar{c}_1$ is obtained via

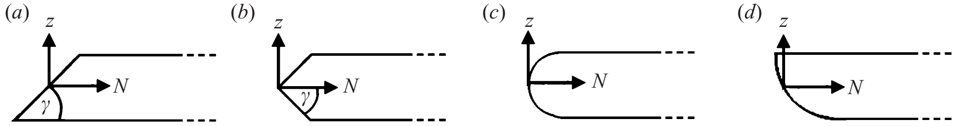

FIGURE 7. Schematic definition of (*a*) trapezoidal and (*b*) hexagonal cross-sections and (*c*) semicircular and (*d*) quarter-circular sidewall geometry.

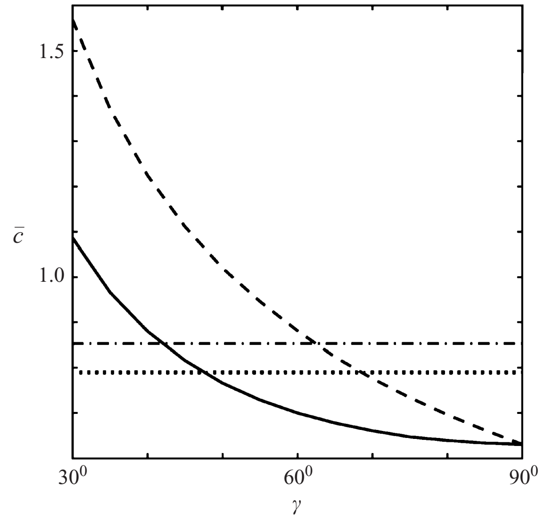

FIGURE 8. Variation with γ of the coefficient $\bar{c}$ quantifying the influence of the sidewalls for hexagonal (dashed line) and trapezoidal (solid line) cross-sections. Also marked are the values of $\bar{c}$ for semicircular ($\approx$0.79, dotted line) and quarter-circular ($\approx$0.85, dash-dotted line) sidewalls.

a numerical solution of the corresponding Dirichlet problems (2.25), (2.26) and (2.28) governing V_s.

REFERENCES

AKBARI, M., SINTON, D. & BAHRAMI, M. 2009 Pressure drop in rectangular microchannels as compared with theory based on arbitrary cross-section. *J. Fluids Engng* **131**, 1–8.

ALBERTONI, S., CERCIGNANI, C. & GOTUSSO, L. 1963 Numerical evaluation of the slip coefficient. *Phys. Fluids* **6**, 993–996.

ARKILIC, E. B., BREUER, K. S. & SCHMIDT, M. A. 2001 Mass flow and tangential momentum accommodation in silicon micromachined channels. *J. Fluid Mech.* **437**, 29–43.

ARKILIC, E. B., SCHMIDT, M. A. & BREUER, K. S. 1997 Gaseous slip flow in long microchannels. *J. Microelctromech. Syst.* **6**, 167–178.

AUBERT, C. & COLIN, S. 2001 High-order boundary conditions for gaseous flows in rectangular microchannels. *Microscale Therm. Engng* **5**, 41–54.

BATCHELOR, G. K. 1967 *An Introduction to Fluid Dynamics*, Cambridge Mathematical Library series. Cambridge University Press.

BESKOK, A., KARNIADAKIS, G. E. & TRIMMER, W. 1996 Rarefaction and compressibility effects in gas microflows. *J. Fluids Engng* **118**, 448–456.

CARRIER, G. F., KROOK, M. & PEARSON, C. E. 1966 *Functions of a Complex Variable*. McGraw-Hill.

CERCIGNANI, C. 2000 *Rarefied Gas Dynamics*. Macmillan.

COLE, J. D., KELLER, H. B. & SAFFMAN, P. G. 1967 The flow of a viscous compressible fluid through a very narrow gap. *SIAM J. Appl. Math.* **15**, 605–617.

van Dyke, M. 1975 *Perturbation Methods in Fluid Mechanics*. Academic.

Ewart, T., Perrier, P., Graur, I. A. & Meolans, J. G. 2007 Mass flow rate measurements in a microchannel, from hydrodynamic to near free molecular regimes. *J. Fluid Mech.* **584**, 337–356.

Gad-El-Hak, M. 1999 The fluid mechanics of microdevices. *J. Fluid Engng* **121**, 5–33.

Gad-El-Hak, M. 2002 *The MEMS Handbook*. CRC press.

Gat, A., Frankel, I. & Weihs, D. 2008 Gas flows through constricted shallow micro-channels. *J. Fluid Mech.* **602**, 427–442.

Graur, I. A., Meolans, J. G. & Zeitoun, D. E. 2005 Analytical and numerical description for isothermal gas flow in microchannels. *Microfluid. Nanofluid.* **2**, 64–77.

Ho, C. M. & Tai, Y. C. 1998 Micro-electro-mechanical-systems (MEMS) and fluid flows. *Annu. Rev. Fluid Mech.* **30**, 579–612.

Jang, J. & Wereley, S. 2004 Pressure distributions of gaseous slip flow in straight and uniform rectangular microchannels. *Microfluid. Nanofluid.* **1**, 41–51.

Kober, H. 1957 *Dictionary of Conformal Representations*. Dover.

Lauga, E., Stroock, A. & Stone, H. 2004 Three-dimensional flows in slowly varying planar geometries. *Phys. Fluids* **16**, 3051–3062.

Lee, W. Y., Wong, M. & Zohar, Y. 2001 Gas flow in microchannels with bends. *J. Micromech. Microengng* **11**, 635–644.

Lee, W. Y., Wong, M. & Zohar, Y. 2002*a* Microchannels in series connected via a contraction/expansion section. *J. Fluid Mech.* **459**, 187–206.

Lee, W. Y., Wong, M. & Zohar, Y. 2002*b* Pressure loss in constriction microchannels. *J. Microelectromech. Syst.* **11**, 236–244.

Lighthill, M. J. 1958 On displacement thickness. *J. Fluid Mech.* **4**, 383–392.

MacInnes, J. M., Du, X. & Allen, R. W. K. 2003 Prediction of electrokinetic and pressure flow in a microchannel T-junction. *Phys. Fluids* **15**, 1992–2005.

Milne-Thomson, L. M. 1968 *Theoretical Hydrodynamics*. Macmillan.

Morini, Gian Luca 2004 Laminar liquid flow through silicon microchannels. *J. Fluids Engng* **124**, 485–489.

Polyanin, A. D. 2002 *Handbook of Linear Partial Differential Equations*. Chapman and Hall.

Qin, F.-H., Sun, D.-J. & Yin, X.-Y. 2007 Perturbation analysis on gas flow in a straight microchannel. *Phys. Fluids* **19**, 1–14.

Sharipov, F. 1999 Rarefied gas flow through a long rectangular channel. *J. Vac. Sci. Technol.* **17**, 3062–3066.

Sharipov, F. 2003 Application of the cercignanilampis scattering kernel to calculations of rarefied gas flows. Part 2. Slip and jump coefficients. *Euro. J. Mech.* B **22**, 133–143.

Sharipov, F. & Seleznev, V. 1998 Data on internal rarefied gas flows. *J. Phys. Chem. Ref. Data* **27**, 657–706.

Sone, Y. 2002 *Kinetic Theory and Fluid Dynamics*. Birkhauser.

Taylor, G. I. & Saffman, P. G. 1957 Effects of compressibility at low Reynolds number. *J. Phys. Chem. Ref. Data* **24**, 553–562.

White, F. M. 1986 *Fluid Mechanics*, 2nd edn. McGraw-Hill.

Wu, H. Y. & Cheng, P. 2003 Friction factors in smooth trapezoidal silicon microchannels with different aspect ratios. *Intl J. Heat Mass Transfer* **46**, 2519–2525.

Wu, H., Wu, X. & Wei, Z. 2009 Flow friction and heat transfer of ethanol–water solutions through silicon microchannels. *J. Micromech. Microengng* **19**, 1–10.

Yu, Z. T. F., Lee, Y.-K., Wong, M. & Zohar, Y. 2005 Fluid flows in microchannels with cavities. *J. Microelctromech. Syst.* **14**, 1386–1398.

Zohar, Y., Lee, S. Y. K., Lee, W. Y., Jiang, L. & Tong, P. 2002 Subsonic gas flow in a straight and uniform microchannel. *J. Fluid Mech.* **472**, 125–151.